P2.6 HYDRAULIC-JUMP ROTORS: FAVORABLE ENVIRONMENTS FOR THEIR FORMATION

R. F. Hertenstein *
Northwest Research Associates
Colorado Research Associates Division
Boulder, CO

J. P. Kuettner
National Center for Atmospheric Research
Boulder, CO

1. INTRODUCTION

Two distinct rotor types have been identified from observations (Lester and Fingerhut 1974) and numerical simulations (Hertenstein and Kuettner 2005, hereafter HK). The first rotor type is associated with a Mountain-Wave/Rotor (MW/R) system comprising resonant waves, while the second MW/R system resembles a hydraulic jump. Using wind and stability profiles based on observations from the 1950s Sierra Wave Project (Grubišič, V., and Lewis 2004), HK perfomed a series of two-dimensional simulations designed to test the sensitivity of shear in the wind profile, especially within a near-mountaintop, upstream inversion. The rotor type that forms was found to be very sensitive to details in the shear profile within the inversion.

The near-mountaintop upstream inversion is characteristic of the mountain wave phenomenon and downslope windstorms. A foehn or cap cloud provides a visual indicator of the inversion as it spills over the lee slope, inspiring the term "cloud waterfall".

Herein we extend the work of HK, and explore the role of inversion strength and height (above mountaintop), as well as mountain height, lee-slope profile, and secondary mountain ranges.

2. EXPERIMENTAL DESIGN

Two-dimensional simulations were performed with the Regional Atmospheric Modeling System (RAMS), which uses the non-hydrostatic, fully compressible governing equations. Complete details regarding model equations, vertical coordinate, grid structure, time and space differencing, as well as available parameterizations (e.g., radiation, turbulence, and microphysics) have been elaborated upon in Pielke et al. (1992), Cotton et al. (2003) and numerous references therein.

A single model grid with horizontal spacing of 150 m was employed over 1700 points. Vertical spacing ranged from 20 m at the lowest level stretching to 150 m to a maximum height of 19.7 km. Horizontally-homogeneous initialization was used. Topography was modeled with the well-known Witch of Agnesi profile. For simulations testing the sensitivity to inversion strength and height, a 40 km half-width on the upstream side and 5 km half-width on the lee side roughly approximate the profile of the Sierra Nevada, especially the lee slope. The mountain top height (H) in the model was set to 2500 m. Details of simulations testing the sensitivity to topographical characterisitics are explained in Section 4.

Initial wind and stability profiles are shown in Fig. 1. The two wind profiles are based on observations taken during the Sierra Wave Project. The first features a constant speed through the inversion (lower inset); these simulations are referred to as having no internal shear. The second wind profile, with winds increasing 8 ms^{-1} through the inversion (upper inset), results in internal shear of $(13.33 \times 10^{-3} s^{-1})$. The inversion depth is 600m in all simulations. Both wind profiles are set with constant shear $(4.29 \times 10^{-3} s^{-1})$ above and below an upstream inversion. For a given flow speed at the bottom of the inversion, wind profiles with relatively weak internal shear produced hydraulic-jump rotors in HK, while relatively strong internal

*Corresponding author address: Rolf F. Hertenstein, Northwest Research Associates - CoRA Division, 3380 Mitchell Lane, Boulder, CO 80301; email: herten@cora.nwra.com.

shear produced resonant-wave rotors.

3. EFFECT OF INVERSION STRENGTH AND HEIGHT

Figure 2 shows isentropes and bulk Richardson number (R_i, shaded) less than 0.25 for a hydraulic-jump MW/R system simulated with $\Delta\theta_i = 11K$ and no internal shear. Characteristics include a splitting inversion, as well as high-reaching and widespread turbulence. Downslope winds (not shown) reach 52 ms^{-1} between 100 m and 400 m above the slope near $x = 12$ km. Winds exceeding 40 ms^{-1} extend more than 30 km from the mountain crest. Between 2.5 and 3.0 hours model integration time, the simulated hydraulic-jump rotor experiences maximum Turbulent Kinetic Energy (TKE) ranging from 10 to almost 50 m^2s^{-2}.

An example of the more-familiar resonant-wave MW/R system is shown in Fig. 3. The initial conditions are as before, with the important exception that the windspeed increases 8 ms^{-1} through the initial inversion, giving an internal shear of $13.3 \times 10^{-3}s^{-1}$. Maximum TKE associated with the resonant-wave rotors is weaker and much less variable, between 9 and 11 m^2s^{-2}. The spatial extent of turbulence, indicated by $R_i < 0.25$ is mostly confined below the mountain-wave crest. Downslope winds (not shown) are weaker than the hydraulic-jump MW/R system, reaching 38 ms^{-1} between $x = 14$ and 17 km. The effect of the wind profile on rotor formation was discussed in detail by HK.

We next performed a series of simulations to explore the effect of inversion strength, measured by the initial upstream potential temperature change ($\Delta\theta_i$) across a near-mountaintop inversion with height (z_i) set to 2700m, or 200m above the mountaintop.

The simulations are summarized in Fig. 4 (see row of symbols corresponding to $z_i = 2700m$ in both panels). For simulations without internal shear (Fig. 4a), $\Delta\theta_i < 7K$ lead to resonant-wave rotors (stars), while simulations with $\Delta\theta_i > 8K$ produce hydraulic-jump rotors (diamonds). By contrast, for simulations with internal shear (Fig. 4b), transition from resonant-wave to hydraulic-jump rotors occurs at much stronger inversion strength, approximately 18K. Thus, hydraulic-jump rotors are unlikely to occur in an environment with relatively strong internal shear and a near-mountaintop inversion.

When $\Delta\theta_i < 5K$, simulations with internal shear produce a structure that we will refer to as lee eddies (triangles in Fig. 4b). The eddies form directly along the lee slope, then break away and propagate downstream. Lee eddies resemble "rotor streaming" (Foerchtgott 1969); however, in contrast to our initial conditions, rotor streaming forms when the wind profile shows a maximum in the vicinity of the mountaintop, with decreasing winds above.

In a second series of simulations we explored the effect of the inversion height above the mountain by first increasing z_i to 3225m and then to 4050m. As z_i increases, hydraulic-jump rotors develop in environments with weaker inversions, especially for simulations with internal shear (Fig. 4b). This indicates that hydraulic-jump rotors are more likely to occur when conditions favor higher inversions.

As z_i/H increases to more than 2.0, the mountain appears to lose some of its influence on the inversion. At $z_i = 5400m$, the presence of internal shear leads to lee eddies for most simulations, and only $\Delta\theta_i = 13K$ produces a resonant-wave rotor (Fig. 4b). Simulations with no internal shear and small $\Delta\theta_i$ produce lee eddies while resonant-wave or hydraulic-jump rotors are produced with stronger inversions.

To understand the dynamic mechanism leading to hydraulic-jump rotors, HK examined horizontal vorticity

$$\eta = \frac{\partial u}{\partial z} - \frac{\partial w}{\partial x}$$

production in the lee of the mountain. As pointed out by HK, hydraulic-jump rotors were associated with negative η produced by baroclinic generation. In a two-dimensional, incompressible Boussinesq system, with $f = 0$,

$$\frac{d\eta}{dt} = B_x + D,$$

where baroclinic generation due to horizontal buoyancy gradients is given by

$$B_x = -g\frac{\partial}{\partial x}\left(\frac{\theta'}{\bar{\theta}}\right),$$

$\theta = \bar{\theta}(z) + \theta'$, and D represents subgrid-scale turbulent stresses. Thus, horizontal vorticity is produced as the initial horizontal inversion with a vertically-oriented θ gradient becomes distorted along the lee slope. For simulations with internal shear, which contain positive η within the initial inversion, greater (more negative) B_x is needed to produce sufficient negative η for hydraulic-jump rotors compared to simulations with no internal shear.

Fig. 5(a) shows minimum B_x within the distorted inversion along the lee slope at $z_i = 2700m$ for several inversion strengths. The simulations show minimum B_x becoming increasingly negative as $\Delta\theta_i$ increases. For simulations with no internal shear (solid line), the threshold for transition from resonant-wave to hydraulic-jump rotors occurs at approximately $B_x = -2.0 \times 10^{-4}s^{-2}$. By contrast, due to the presence of initial positive η, simulations with internal shear require $B_x = -4.0 \times 10^{-4}s^{-2}$ for the formation of hydraulic-jump rotors.

Baroclinic generation at $z_i = 5400m$ is weak for all simulations with internal shear (Fig. 5b). Simulations with no internal shear only produce hydraulic-jump rotors when $B_x < -2.0 \times 10^{-4} s^{-2}$, as was the case at $z_i = 2700m$.

We further investigated characteristics of the simulated MW/R system, using two metrics: rotor height and rotor turbulence.

Figure 6a shows rotor height for two inversion heights ($z_i = 2700m$ - thin lines, and $z_i = 4050m$ - thick lines) and for simulations with (dashed lines) and without (solid lines) internal shear. For resonant-wave rotors (stars), rotor height increases as $\Delta\theta_i$ increases, regardless of internal shear. In addition, regardless of internal shear, higher resonant-wave rotors occur with higher inversions. Our results are in agreement with those of Corby and Wallington (1956), who showed that resonant-wave amplitude increased as a lower-layer stability (in a two- or three-layer model) tended toward a sharp inversion. By contrast, for hydraulic-jump rotors (diamonds), rotor height generally *decreases* as $\Delta\theta_i$ increases, with or without internal shear. Hydraulic-jump rotors do not always produce the highest-amplitude rotors - those are produced by simulated resonant-wave rotors without internal shear, and $z_i = 4050m$ (thick, solid lines).

Rotor turbulence, measured by maximum Turbulent Kinetic Energy (TKE) generally increases with increasing $\Delta\theta_i$ (Fig. 6b). Simulations without internal shear (solid lines) result in stronger turbulence than those with internal shear (dashed lines). In addition, most, but not all, hydraulic-jump rotors are associated with stronger turbulence. The highest amplitude MW/R systems (Fig. 6a) do not produce the greatest turbulence.

4. THE ROLE OF TOPOGRAPHY

Several simulations were performed to explore the role of topography on rotor formation. In the first set of experiments, the height of the mountain barrier was lowered (from $2500m$ to $500m$, in steps of $500m$), while the lee-slope half-width (5 km) remained unchanged, leading to a progressively shallower lee slope. The wind profile was as before, and both profiles with and without internal shear were tested. As expected, with shallow slopes, the baroclinic generation of negative vorticity was not sufficient to produce hydraulic-jump rotors. As the slope becomes increasingly shallow, resonant waves display lower amplitude, longer wavelength, and weaker rotors.

In a second set of simulations, mountain height was again systematically lowered, but the half-width of the lee slope was adjusted to maintain a steep lee slope. Using the same wind profile as previously, once again only resonant-wave rotors formed.

A third set of simulations were run in which a steep lee slope was maintained, but the wind speed at all levels was adjusted downward as mountain height decreased. Most experiments once again produced resonant-wave rotors. However, one experiment using a $1250m$ mountain height, an inversion at $z_i = 2500m$ with $\Delta\theta_i = 15K$, and a wind profile with 10 ms^{-1} at all levels, produced a system with some of the characteristics of a hydraulic-jump rotor. The jump occurs near the mountain crest, and to our knowledge, this has not been observed in nature.

Lastly, several simulations were run in which the topography was modified by the addition of a second mountain range downstream of the primary range, representing of the Sierra Nevada Mountains with the Inyo Mountains further east. The wind and stability profiles were the same as used in the $z_i = 2700m$, no internal shear simulations. While using a single mountain range results in a hydraulic-jump rotor (Fig. 2), the addition of the Inyo Mountains produced a resonant-wave rotor (Fig. 7). Work is ongoing to better understand the role of the downstream mountain range.

5. CONCLUSIONS

We have extended the work of Hertenstein and Kuettner (2005), and have examined the role of inversion strength and height in rotor formation, with special attention to factors leading to hydraulic-jump rotors. In addition, we have explored how mountain height, the lee-slope profile, and secondary mountain ranges influence rotor development.

Our main findings are as follows:

1. Lack of vertical shear within the upstream inversion favors the prevalence of hydraulic-jump rotors (Fig. 4). Vertical shear within the upstream inversion leads to resonant-wave rotors, unless the inversion is strong.

2. Strong inversions lead to hydraulic-jump rotors, regardless of shear within the inversion. (Fig. 4).

3. Hydraulic-jump rotors are more likely to occur in the presence of higher inversions (Fig. 4). Very high inversions produce fewer rotors, especially if vertical shear within the inversion is present.

4. For hydraulic-jump rotors, rotor height decreases as inversion strength increases (diamonds, Fig. 6a). By contrast, for resonant-wave rotors, rotor height increases as inversion strength increases (stars, Fig. 6a).

5. Rotor turbulence increases as inversion strength increases (Fig. 6b). Hydraulic-jump rotors usually, but not always, produce greater turbulence.

6. Increasing the height and steepness of the lee slope favors the prevalence of hydraulic-jump rotors. The addition of a second mountain range downstream dramatically alters the mountain-wave/rotor system (cf. Figs. 2 and 7).

The potential for high-amplitude mountain waves is relatively easy to forecast. The important parameters given a quasi-two-dimensional mountain range or ridgeline are flow nearly perpendicular to the range (at least 10 ms^{-1} at mountaintop), wind increasing with height above mountaintop, and stable static stability, preferably with the presence of a near-mountaintop inversion (OSTIV 1993). The experience of the aviation community, especially glider pilots, tells us that rotors are almost always present when high-amplitude mountain waves exist. Thus, the presence of rotor activity is also not difficult to forecast. However, the results presented here and in HK underscore the difficulty in forecasting rotor details (e.g., type, height, turbulence intensity), because of precise knowledge of the upstream wind and stability profiles that is required. Our qualitative examination of standard twice-daily radiosonde data upstream of the Colorado Rocky Mountains leads us to believe that necessary details are sometimes captured by the observations. However, soundings from operational numerical model forecasts at present appear insufficient for detailed rotor forecasts. Increased vertical resolution in operational models should prove useful to forecasters in predicting details of rotor flow.

6. References

Cotton W.R., R.A. Pielke, Sr., R.L. Walko, G.E. Liston, C.J. Tremback, H. Jiang, R.L. McAnelly, J.Y. Harrington, M.E. Nicholls, G.G. Carrio, and J.P. Mcfadden 2003: RAMS 2001: Current status and future directions. *Meteorol. Atmos. Phys.*, **82**, 5-29.

Corby, G.A., and C.E. Wallington 1956: Airflow over moutnains: The lee-wave amplitude. *Q.J.R. Meteorol. Soc.*, **82**, 266-274.

Foerchtgott, J., 1949: Evidence for mountain-sized lee eddies. *Weather*, **24**, 255-260.

Grubišič, V., and J.M. Lewis 2004: Sierra Wave Project revisited: 50 years later. *Bull. Am. Meteorol. Soc.*, **85**, 1127-1142.

Hertenstein, R.F., and J. P. Kuettner, 2005. Rotor types associated with steep lee topography: Influence of the wind profile. *Tellus*, **47**, 310-326.

Kuettner, J.P., 1959: The rotor flow in the lee of the mountains. Geophysics Research Directorate (GRD) Research Notes 6, AFCRC-TN-58-626, Air Force Cambridge Research Center, USA, 20 pp.

Lester, P.F., and W.A. Fingerhut 1974: Lower turbulent zones associated with lee waves. *J. Appl. Meteorol.*, **13**, 54-61.

OSTIV 1993: Handbook of Meteorological Forecasting for Soaring Flight, 2nd Edition, Technical Note No. 158, World Meteorological Organization, Geneva, Switzerland, 85 pp.

Pielke, R.A., W.R. Cotton, R.L. Walko, C.J. Tremback, W.A. Lyons, L.D. Grasso, M.E. Nicholls, M.D. Moran, D.A. Wesley, T.J. Lee, and J.H. Copeland 1992: A comprehensive meteorological modeling system - RAMS. *Meteorol. Atmos. Phys.*, **49**, 69-91.

Acknowledgements

This work was supported by the National Science Foundation under grant number NSF-0233165.

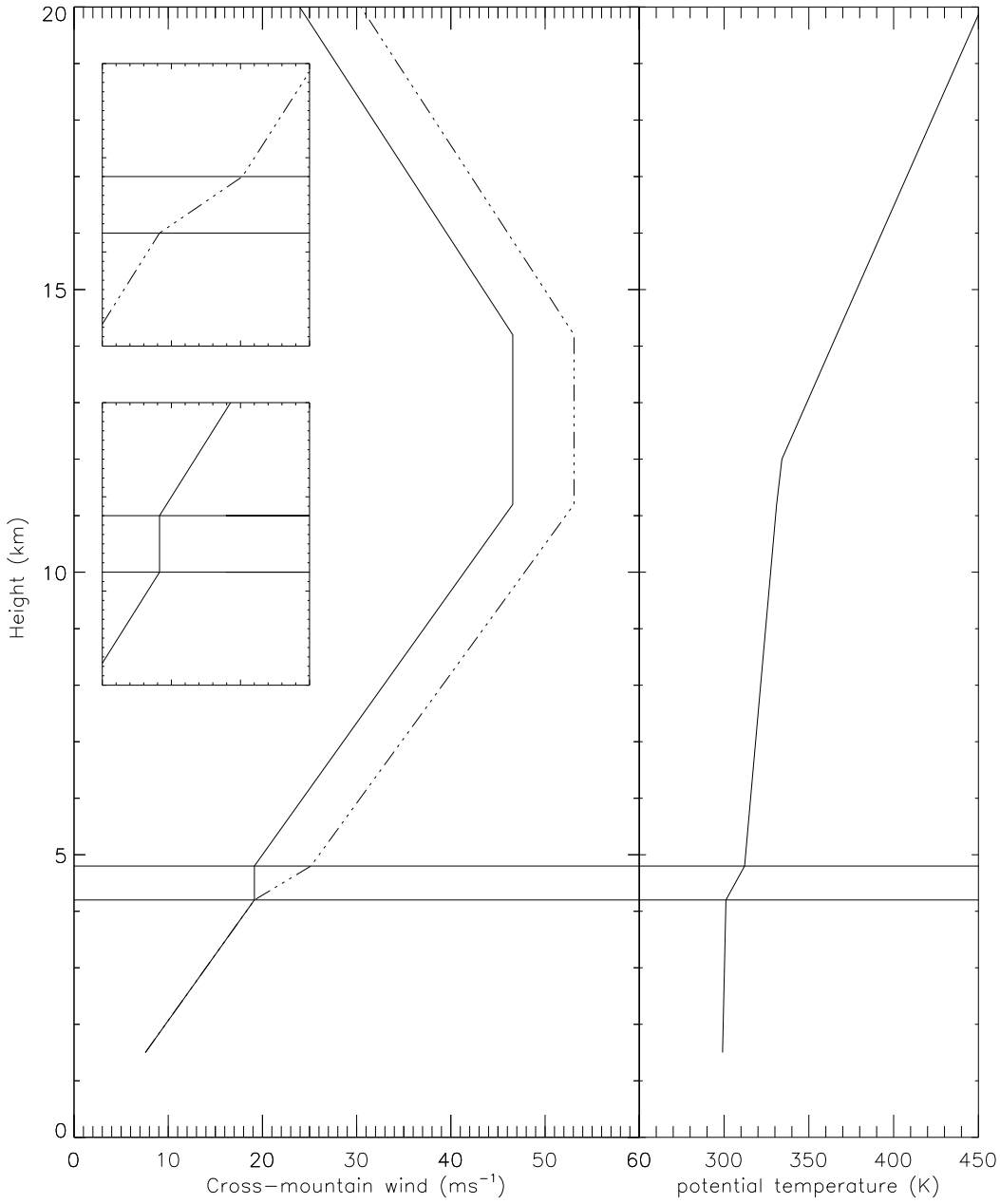

Figure 1: Initial wind profiles (left side) for simulations with no internal shear (solid line) and with internal shear (dashed line). Insets show details of the wind profile near the inversion, bounded by horizontal lines. The figures shows the case in which the inversion is just above $4000m$. Initial potential temperature profile is shown in the right panel.

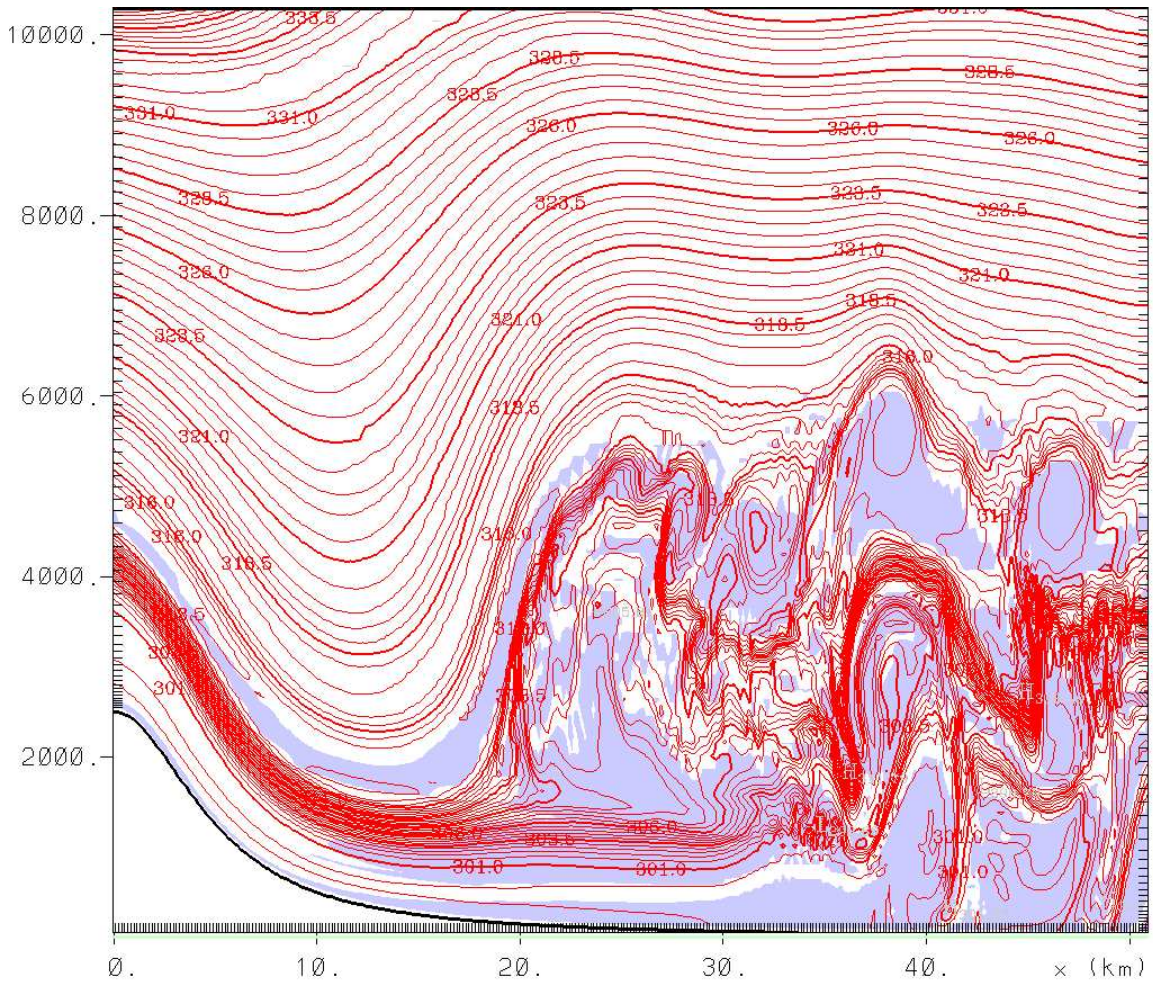

Figure 2: Potential temperature (contours, interval 0.5K), and Bulk Richardson Number (values less than 0.25 shaded) for the simulation of a hydraulic-jump rotor.

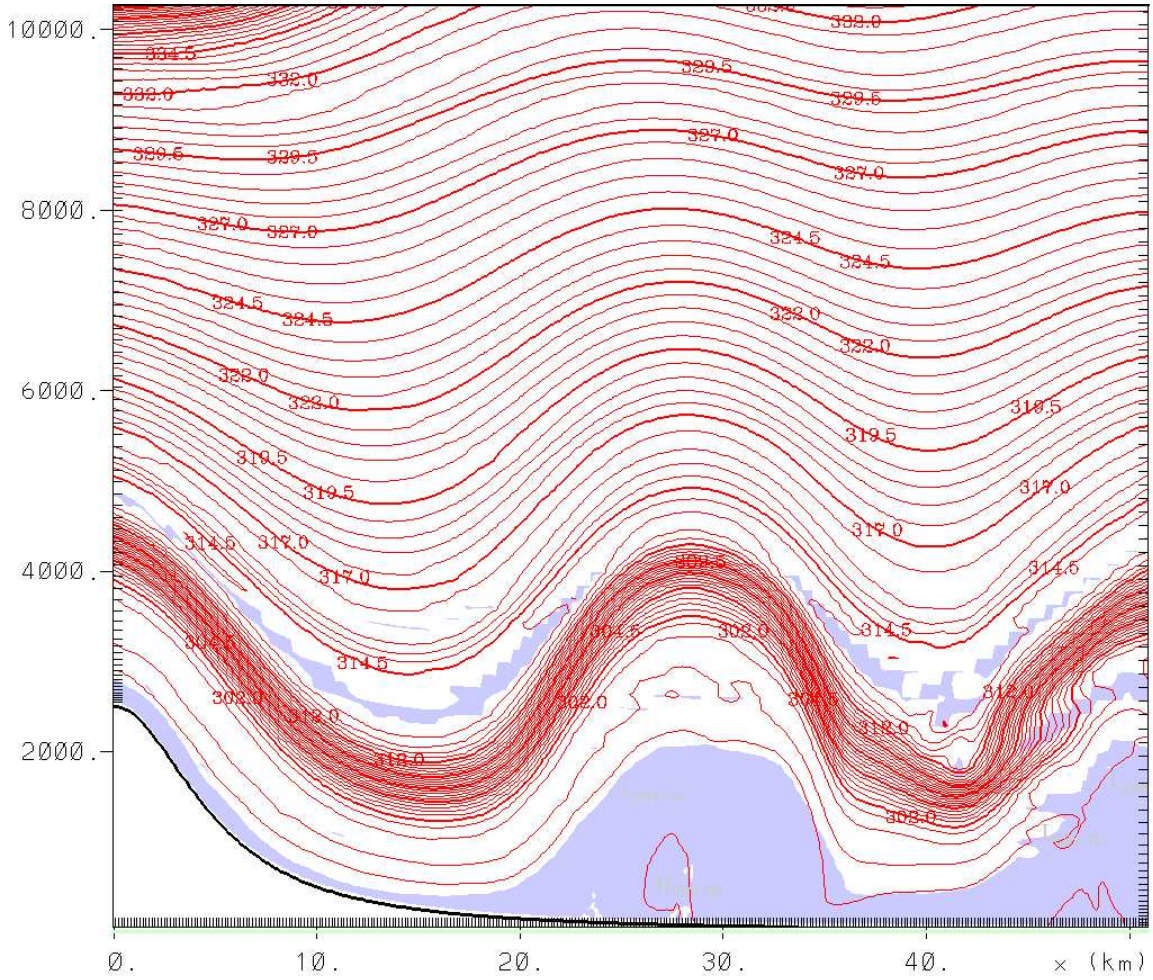

Figure 3: Potential temperature (contours, interval 0.5K), and Bulk Richardson Number (values less than 0.25 shaded) for the simulation of a resonant-wave rotor.

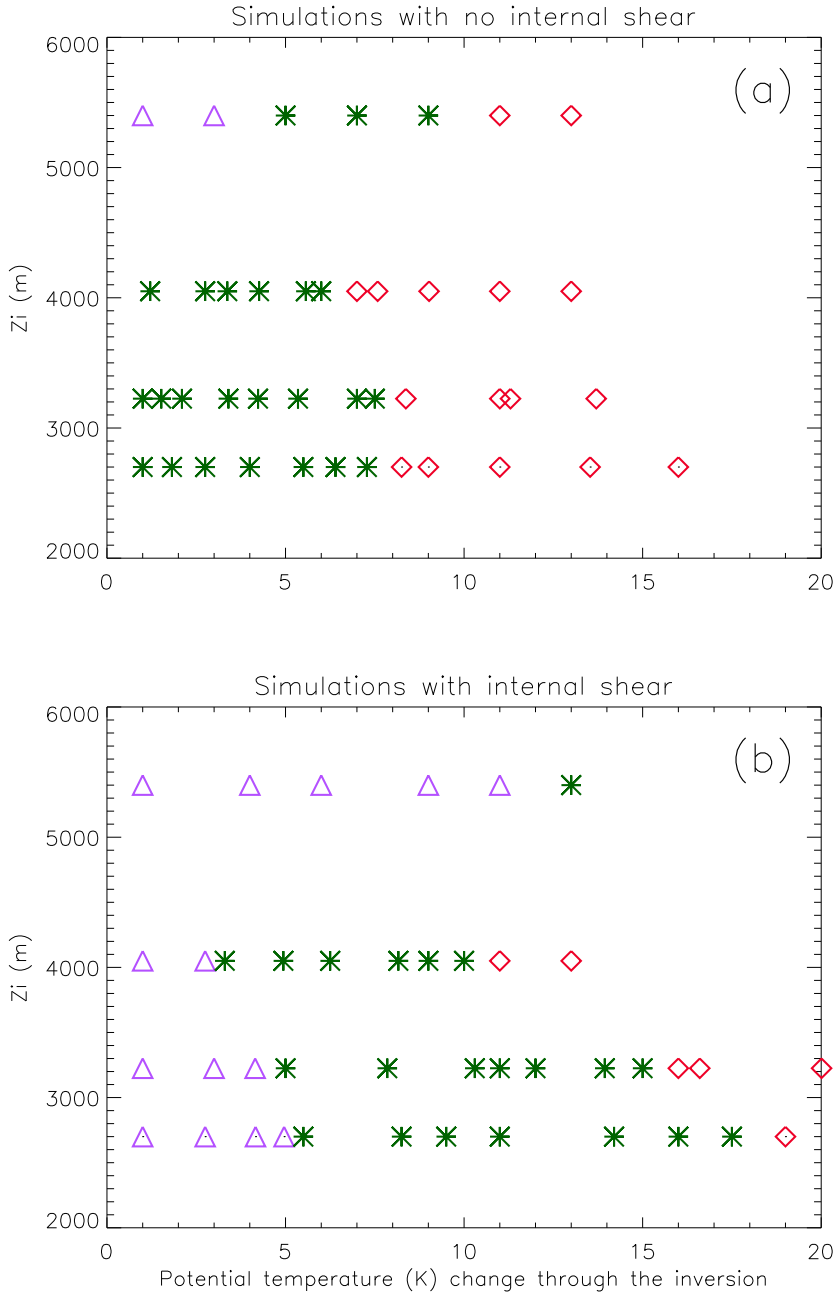

Figure 4: (a) Inversion height vs. inversion strength for simulations with no internal shear. Symbols: stars indicate resonant-wave rotors, diamonds show hydraulic-jump rotors, while lee eddies are represented by triangles. (b) as in (a) except for simulations with internal shear.

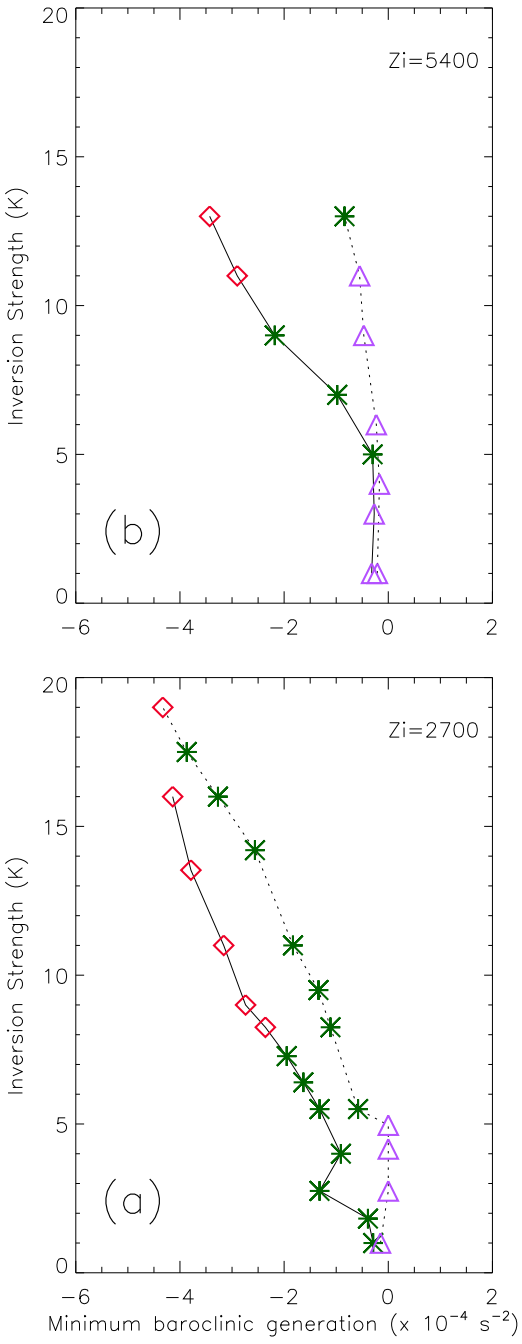

Figure 5: Inversion strength vs. minimum baroclinic generation for simulations (a) at $z_i = 2700m$, and (b) at $z_i = 5400m$. Solid lines connect simulations with no internal shear, while dashed lines connect simulations with internal shear. Symbols are as in Figure 4. Note that (a) is the *lower* panel, while (b) is the *upper* panel in this figure.

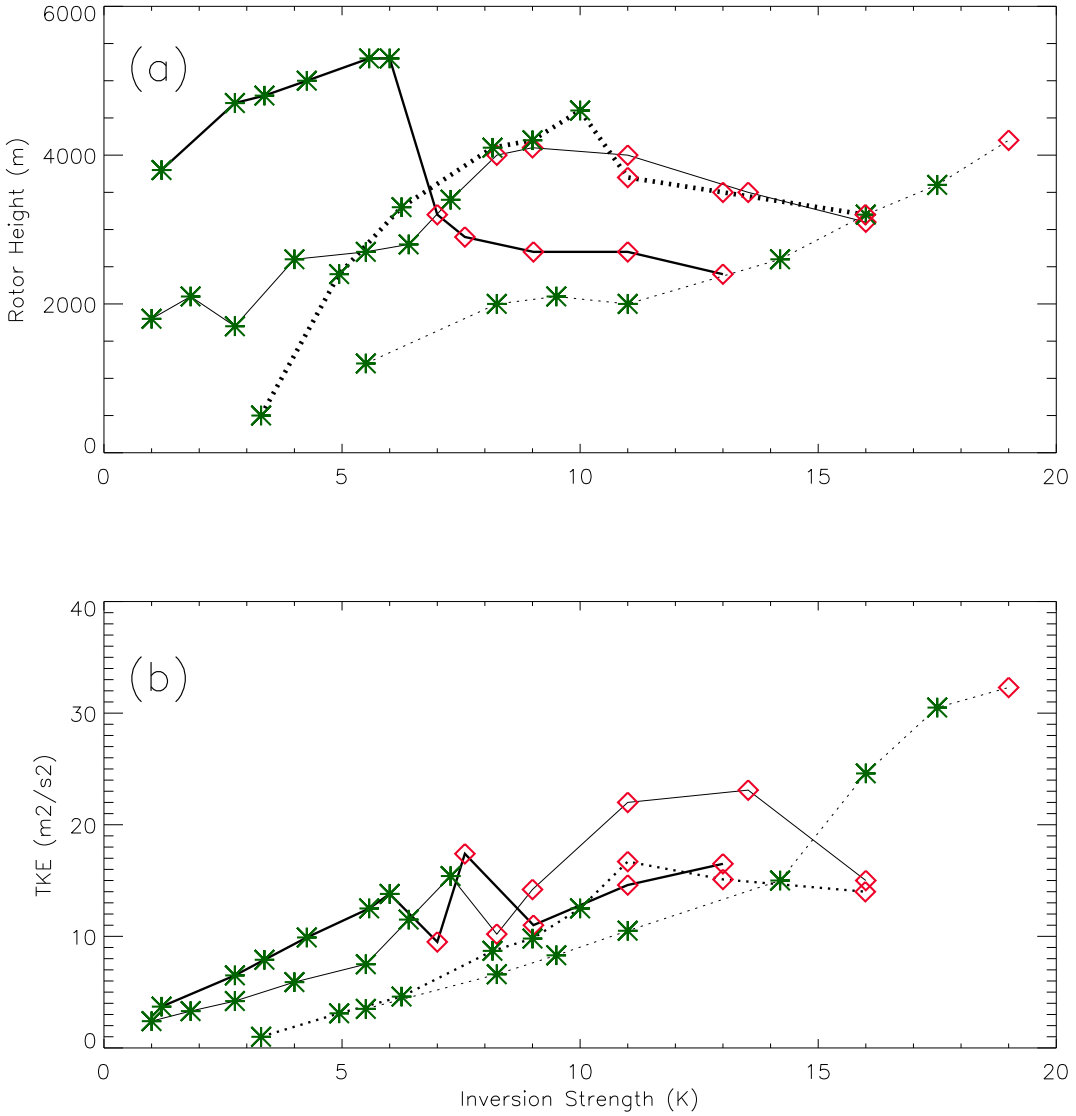

Figure 6: (a) Rotor height vs. inversion strength, and (b) Maximum Turbulent Kinetic Energy vs. inversion strength. Solid lines are simulations with no internal shear, while dashed lines are simulations with internal shear. Symbols are as in Figure 4. Two levels are shown: thin lines (solid or dashed) show simulations at $z_i = 2700m$, while thick lines show simulations at $z_i = 4050m$.

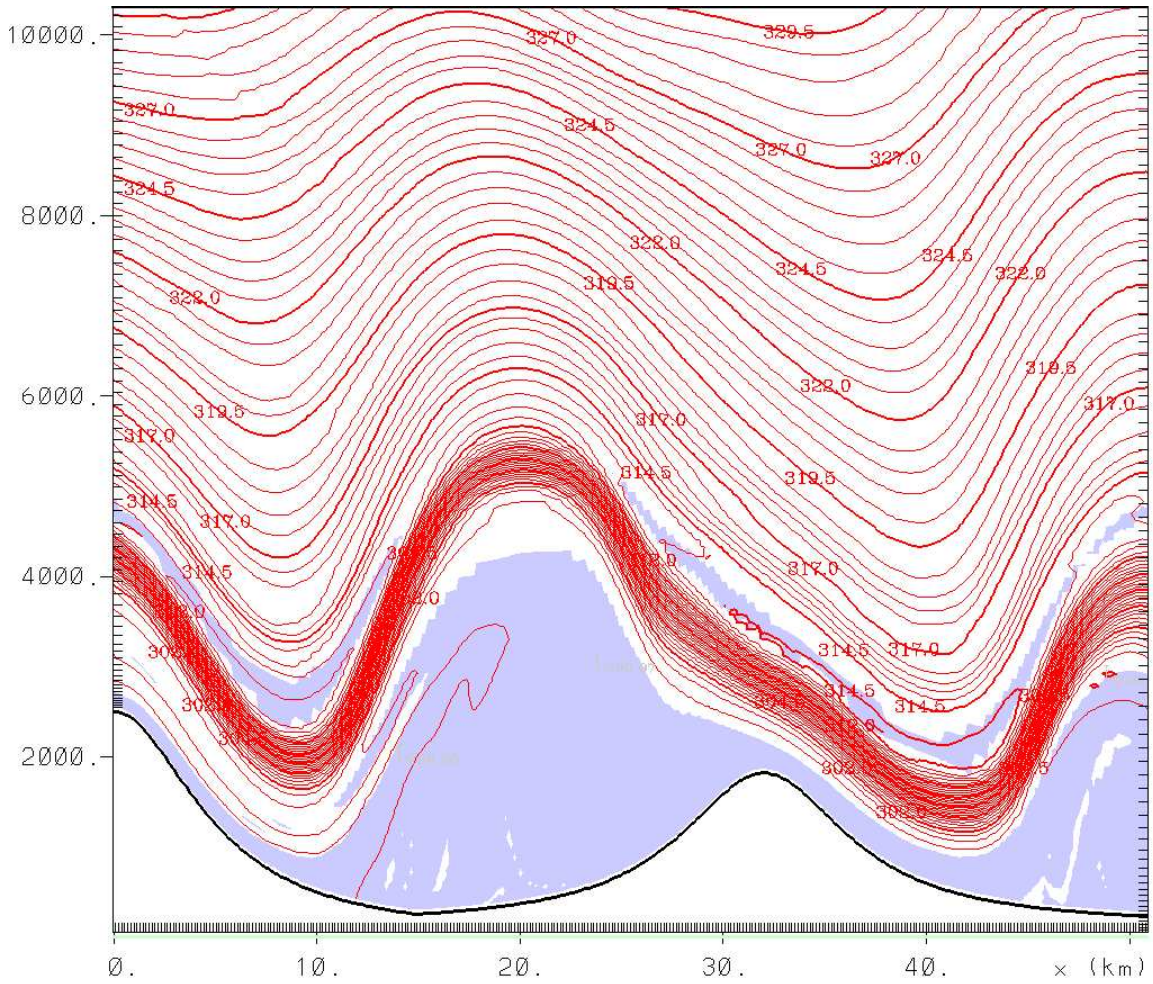

Figure 7: Potential temperature (contours, interval 0.5K), and Bulk Richardson Number (values less than 0.25 shaded) for the simulation using identical initial conditions as Fig. 2, except with the addition of a downstream mountain range